Review: MR Physics for Clinicians

Hyperpolarized ^{13}C Metabolic Imaging Using Dissolution Dynamic Nuclear Polarization

CME

Ralph E. Hurd, PhD,[1*] Yi-Fen Yen, PhD,[1] Albert Chen, PhD,[2] and Jan Henrik Ardenkjaer-Larsen, PhD[3]

This article is accredited as a journal-based CME activity. If you wish to receive credit for this activity, please refer to the website: www.wileyhealthlearning.com

ACCREDITATION AND DESIGNATION STATEMENT

Blackwell Futura Media Services designates this journal-based CME activity for a maximum of 1 *AMA PRA Category 1 Credit*™. Physicians should only claim credit commensurate with the extent of their participation in the activity.

Blackwell Futura Media Services is accredited by the Accreditation Council for Continuing Medical Education to provide continuing medical education for physicians.

EDUCATIONAL OBJECTIVES

Upon completion of this educational activity, participants will be better able to describe the basic physics of dissolution dynamic nuclear polarization (dissolution-DNP), and the impact of the resulting highly nonequilibrium spin states, on the physics of magnetic resonance imaging (MRI) detection.

ACTIVITY DISCLOSURES

No commercial support has been accepted related to the development or publication of this activity.

Faculty Disclosures:

The following contributors have no conflicts of interest to disclose:

Editor-in-Chief: C. Leon Partain, MD, PhD

CME Editor: Scott B. Reeder, MD, PhD

CME Committee: Scott Nagle, MD, PhD, Pratik Mukherjee, MD, PhD, Shreyas Vasanawala, MD, PhD, Bonnie Joe, MD, PhD, Tim Leiner, MD, PhD, Sabine Weckbach, MD, Frank Korosec, PhD

Authors: Ralph E. Hurd, PhD, Yi-Fen Yen, PhD, Albert Chen, PhD, Jan-Henrik Ardenkjaer-Larsen, PhD

This manuscript underwent peer review in line with the standards of editorial integrity and publication ethics maintained by *Journal of Magnetic Resonance Imaging*. The peer reviewers have no relevant financial relationships. The peer review process for *Journal of Magnetic Resonance Imaging* is double-blinded. As such, the identities of the reviewers are not disclosed in line with the standard accepted practices of medical journal peer review.

Conflicts of interest have been identified and resolved in accordance with Blackwell Futura Media Services's Policy on Activity Disclosure and Conflict of Interest. No relevant financial relationships exist for any individual in control of the content and therefore there were no conflicts to resolve.

INSTRUCTIONS ON RECEIVING CREDIT

For information on applicability and acceptance of CME credit for this activity, please consult your professional licensing board.

This activity is designed to be completed within an hour; physicians should claim only those credits that reflect the time actually spent in the activity. To successfully earn credit, participants must complete the activity during the valid credit period.

Follow these steps to earn credit:

- Log on to www.wileyhealthylearning.com
- Read the target audience, educational objectives, and activity disclosures.
- Read the article in print or online format.
- Reflect on the article.
- Access the CME Exam, and choose the best answer to each question.
- Complete the required evaluation component of the activity.

This activity will be available for CME credit for twelve months following its publication date. At that time, it will be reviewed and potentially updated and extended for an additional period.

[1]GE Healthcare, Menlo Park, California, USA.
[2]GE Healthcare, Toronto, Canada.
[3]GE Healthcare, Denmark.
*Address reprint requests to: R.E.H., GE Healthcare, 333 Ravenswood Ave., Menlo Park, CA 94025. E-mail: ralph.hurd@ge.com
Received November 15, 2011; Accepted June 10, 2012.
DOI 10.1002/jmri.23753
View this article online at wileyonlinelibrary.com.

© 2012 Wiley Periodicals, Inc.

This article describes the basic physics of dissolution dynamic nuclear polarization (dissolution-DNP), and the impact of the resulting highly nonequilibrium spin states, on the physics of magnetic resonance imaging (MRI) detection. The hardware requirements for clinical translation of this technology are also presented. For studies that allow the use of externally administered agents, hyperpolarization offers a way to overcome normal magnetic resonance sensitivity limitations, at least for a brief T_1-dependent observation window. A 10,000–100,000-fold signal-to-noise advantage provides an avenue for real-time measurement of perfusion, metabolite transport, exchange, and metabolism. The principles behind these measurements, as well as the choice of agent, and progress toward the application of hyperpolarized ^{13}C metabolic imaging in oncology, cardiology, and neurology are reviewed.

Key Words: hyperpolarized ^{13}C; DNP; metabolic imaging; pyruvate
J. Magn. Reson. Imaging 2012;36:1314–1328.
© 2012 Wiley Periodicals, Inc.

HYPERPOLARIZED ^{13}C magnetic resonance spectroscopic imaging (MRSI) has recently progressed beyond a substantial number of very exciting preclinical studies, into man (1). The goal of this article is to introduce the basic principles and progress that have been made toward the clinical application of hyperpolarized ^{13}C using dissolution dynamic nuclear polarization (DNP). Topics include the significant contributions to the science of dissolution-DNP, rapid multinuclear spectroscopic imaging methods, and animal model work targeted at a wide variety of potential indications.

In MR, hyperpolarization indicates that the polarization is no longer determined by the static magnetic field of the scanner. The enhanced polarization of the agent is created outside the imaging system by means of a polarizer. Hyperpolarization can be based on several principles (2–4). One such is the dissolution-DNP method that has been very successful over the past 5–10 years in terms of making solutions of biologically interesting molecules with highly polarized nuclear spins. The method takes advantage of DNP in the solid state followed by rapid dissolution in a suitable solvent (2–4). The polarization is retained almost completely in the dissolution step, creating a solution with a nonthermal nuclear polarization approaching unity.

To take advantage of a hyperpolarized liquid state solution requires rapid transfer into the subject, as illustrated in Fig. 1, followed by efficient and rapid ^{13}C spectroscopic imaging sequences.

Hyperpolarization by the Dissolution-DNP Method

DNP was first described theoretically by Overhauser in 1953 (5), and a few months later demonstrated by Carver and Slichter (6) in metallic lithium. Overhauser predicted that saturating the conduction electrons of a metal would lead to a dynamic polarization of the nuclear spins. This was a fundamental discovery causing disbelief at the time: that heating of one spin system could lead to the cooling of another. The prediction by Overhauser for metals was extended to electron spins in solution by Abragam (7), and most nuclear magnetic resonance (NMR) spectroscopists are today familiar with the nuclear and electronic Overhauser effect. However, this effect is limited to solutions where relaxation processes couple the spin systems via molecular motions. Soon after, the Solid Effect was described for spins in the solid state coupled by dipolar interactions (8). Later, DNP in the solid state was extended mechanistically to processes involving several electron spins (thermal mixing) (9). The theory of DNP in the solid state, however, has failed to provide a quantitative description of the general case. In the solid state, the high electron spin polarization is in part transferred to the nuclear spins by microwave irradiation close to the resonance frequency of the electron spin. The efficiency of this process depends on several parameters characterizing the various spin systems, but also on technical factors such as microwave frequency and power.

DNP has mainly been applied to the generation of polarized targets for neutron scattering experiments, and it has been demonstrated that the nuclear polarizations of ^{1}H and ^{13}C could be increased to almost 100% and to ~50%, respectively, in the solid state by means of DNP at low temperature (10,11). The mechanism requires the presence of unpaired electrons (electron paramagnetic agent; EPA), which are added to the sample as, for example, an organic radical. The magnetic moment of the electron is 658 times higher than that of the proton. This means that the electron spin will reach unity polarization at a moderate magnetic field strength and liquid helium temperature. At, eg, 3.35 T and 1 K the electron spin polarization is 98%.

DNP Sample Preparation

The first step of hyperpolarizing a new molecule by the dissolution-DNP method is to add unpaired electron spins to the sample. Unpaired electron spins with well-defined properties are most conveniently provided by chemical doping. In order for the DNP process to be effective, the EPA agent must be homogeneously distributed within the sample. Many molecules will be crystalline, or have a tendency to crystallize as saturated aqueous solutions. This will cause the EPA to concentrate in domains and lead to a poor DNP effect. To prevent this, the sample should stay amorphous when frozen to ensure homogenous distribution of the EPA. Three examples of molecules that are liquids at room temperature and stay amorphous when frozen without additives are [1-^{13}C]pyruvic acid (or any other isotopic labeling), 2-keto-[1-^{13}C]isocaproic acid, and *bis*-1,1-(hydroxymethyl)-[1-^{13}C]cyclopropane-d_8(HP001). All three molecules are liquids at room temperature and dissolve well a hydrophilic EPA. For other compounds it is necessary to prevent crystallization by mixing or dissolving the compound

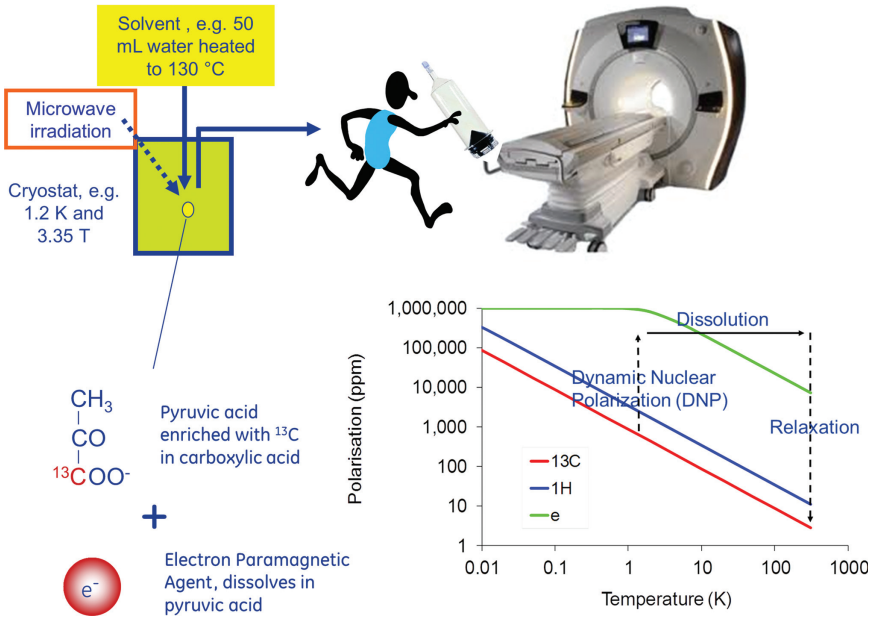

Figure 1. The principle of dissolution-DNP. At room temperature and, eg, 3 T the ^{13}C nuclear spins are only weakly polarized to about 0.00025%, lower right graph. However, an electron spin has a 2700 times stronger magnetic moment and these spins are easily polarized. When the sample is cooled the electron spin polarization of the EPA can reach almost 100%. By irradiation with microwaves close to the resonance frequency of the electron spins, electron-nuclear transitions are induced, and the nuclear spin polarization will be enhanced hundred-fold by DNP, raising the ^{13}C spins to a robust polarization of over 40%. This process is slow and takes typically 15–60 minutes. When the sample is polarized it can be dissolved in, eg, heated water or a buffer, and within seconds a room temperature solution of the hyperpolarized molecule is obtained. The hyperpolarized nuclear spins relax to thermal equilibrium (0.00025%) with a time constant (T_1) of typically 40–80 seconds for carboxylic acids. Therefore the hyperpolarized sample has to be quickly carried to the scanner, injected, and imaged.

in a suitable solvent such as glycerol, or dimethylsulfoxide (DMSO) can be used as solvent for the molecule and the EPA. For in vivo studies it is necessary to be able to formulate the molecule in a concentrated form in order to achieve a high concentration of the molecule after dissolution. To give an estimate of the requirements, a patient dose of 0.1 mmol/kg body weight can be assumed, requiring ~10 mmol of compound, or 1 g with a molecular weight of 100 g/mol. The consequence is that 30%–50% solubility is needed in order to keep the sample size reasonable (see clinical polarizer description). A solvent mixture with high solubility for the molecule and EPA, preventing sample crystallization and with good in vivo tolerance therefore has to be chosen. A good example of a biologically compatible formulation is fumaric acid (eg, [1,4-$^{13}C_2$, 2,3-D_2]fumaric acid) in DMSO. DMSO is a widely used solvent for pharmaceuticals and has a good safety profile (12). It will, however, crystallize when frozen (dry DMSO; melting point 16°C). However, this does not prevent the use of DMSO as solvent for fumaric acid. As saturated solution with a molarity of 3.6 mol/L or 1:1.8 by weight, the solution forms an amorphous solid when frozen. When using DMSO as a glassing agent, care should be taken to ensure the DMSO stays dry (hygroscopic), as small amounts of water will decrease solubility and increase supersaturation.

Another means of improving the solubility involves changing the counterion of salts. Solubility typically increases with increasing size of the counterion, and two examples of this can be mentioned: The cesium salt of bicarbonate ($CsH^{13}CO_3$ (13)), and the TRIS salt of acetate (14). Both of these salts have higher solubility than their sodium counterpart. Finally, for amino acids (zwitter ions at neutral pH) it has shown that either high or low pH preparations increase the aqueous solubility by reducing the charge of the molecule to a point (15) that no or little glycerol is needed to form an amorphous sample.

Electron Paramagnetic Agent (EPA)

The source of the unpaired electron is typically an organic radical, but a few metal ions have been employed successfully for DNP, Cr(V) in particular (16). The choice of EPA will depend on a number of factors. First, the EPA needs to be chemically stable and dissolve readily in the matrix of interest. Second, the electron paramagnetic resonance (EPR) spectrum of the radical should have a width that allows DNP to be effective for the nucleus of interest, ie, a line width that exceeds the Larmor frequency of the nuclear spin. In practice the above criteria mean that two classes of EPA are available, namely nitroxides (17,18) and trityls (19–21). The nitroxides belong to a class of molecules that have been studied extensively by EPR, and which have been used for DNP for many samples. Nitroxides are characterized by having a broad EPR spectrum. The EPR line width is 4.0 per mil (‰) of the EPR frequency, compared to the ^1H resonance frequency, which is 1.5‰ of the EPR frequency. Some of

them have reasonable chemical stability and come with different degrees of hydrophilicity. Another class of EPA with superior properties for direct polarization of low gamma nuclei such as ^{13}C, ^{15}N, and ^{2}H is the trityl. These radicals have a line width that is only 0.80‰ (22,23) of the resonance frequency, much less than the proton resonance frequency, but perfectly matched for ^{13}C, which has a resonance frequency which is 0.37‰ of the EPR frequency. The trityls also exist with a range of hydrophilicities and some of them are chemically very stable.

It has been shown that gadolinium (Gd) can positively affect the solid state DNP enhancement (24). Other paramagnetic ions and molecules (Mn^{2+} and O_2) can in part have the same effect. The physics is not yet understood, but Ardenkjaer-Larsen et al (24) showed that the longitudinal relaxation time of the EPA is shortened by the presence of the Gd ions. The effect of adding 1–2 mmol/L Gd^{3+} is a 50%–100% improvement of the DNP enhancement factor. The effect seems to be general to most samples, but has to be optimized for each sample similarly to the concentration of the EPA. There is no direct DNP effect of the Gd^{3+} by itself under the conditions typically used. Finally, Gd^{3+} may enhance the solid state polarization by DNP, but care should be taken in avoiding accelerated relaxation in the liquid state. Free Gd ions would cause detrimental liquid state relaxation and pose an in vivo safety risk. After dissolution the low concentration of radical and chelated Gd will have a negligible effect on T_1 in most cases.

DNP Instrumentation

Most solid-state DNP has been performed at magnetic fields between 0.35 T (25) and 16.5 T (26,27), and at temperatures from a few hundred mK to room temperature. At temperatures below a few Kelvin and magnetic field strengths above a few Tesla, electron spins are almost fully polarized, and large nuclear polarizations can be obtained. Unlike solid-state NMR spectroscopy applications where nonequilibrium polarizations can be regenerated by repeating the microwave irradiation and NMR acquisition, the polarization generated for in vivo applications will decay irreversibly after dissolution. Hence, the goal is to generate polarizations close to unity. It is therefore important to choose initial operating conditions that have been proven to provide high nuclear polarization, but are at the same time easily achievable using standard instrumentation. Temperatures of ~1 K can be achieved by pumping on liquid helium. In the original dissolution-DNP polarizer design the liquid helium was supplied to the sample space through a needle valve from the magnet cryostat, but in a recent publication an alternative arrangement that used a separate helium dewar was described (28). A magnetic field strength of 3.35 T was chosen since microwave sources are readily available at 94 GHz for irradiation of the electron spin. However, recently it has been demonstrated that for both nitroxides and trityls a significant improvement in polarization can be obtained by increasing the magnetic field strength (29,30) or lowering the temperature (31). For the

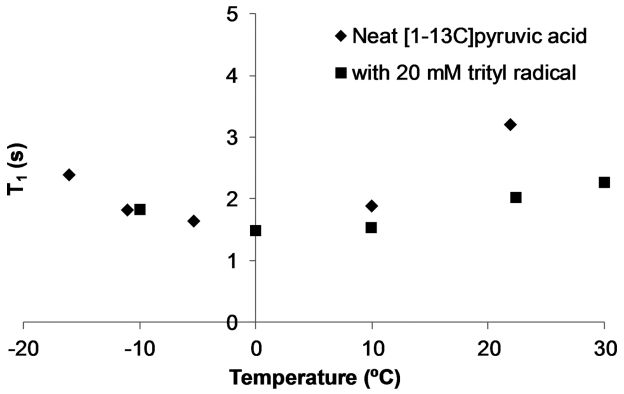

Figure 2. Longitudinal relaxation time, T_1, as a function of temperature for neat [1-^{13}C]pyruvic acid with ■ and without ◆ 20 mmol/L trityl.

compound [1-^{13}C]pyruvic acid, the ^{13}C polarization improved from 27% at 3.35 T to 60% at 4.64 T in the solid state. The literature has been limited and disagrees on the magnetic field dependence of DNP (32). On the other hand, it has been well established that lowering the temperature is beneficial for DNP.

Dissolution and Relaxation in the Liquid State

To make the polarized solid sample useful for in vivo imaging, it needs to be dissolved in a suitable buffer. Depending on the solid sample preparation the dissolution may involve neutralization of the agent with acid or base. Buffering of the solution may be required to maintain control of pH within the physiologic range of 6.8 to 8.1. Physiological buffers such as Tris(hydroxymethyl)aminomethane (TRIS) or 4-(2-hydroxyethyl)piperazine-1-ethanesulfonate (HEPES) are commonly used. Attention to the tonicity of the formulation should be paid and close to isotonic is desired. This may mean lowering the concentration of solutes after dissolution by dilution or adding sodium chloride to the dissolution medium. The dissolution has to be efficient and fast compared to the nuclear T_1 in order to preserve the nuclear polarization in this process. Formulating the solid sample as beads or powder may improve the dissolution (in terms of polarization and recovery of the solid sample), but understanding and optimizing the fluid dynamics (33) as well as providing the necessary heat is essential for optimal performance of more difficult agents. Relaxation during the dissolution process can depend on several factors. To minimize relaxation, dissolution is performed inside the cryostat in the high field of the polarizer (eg, ~3 T in the case of a 3.35 T polarizer), but above the liquid helium surface. Any paramagnetic ions that could increase the relaxation rate are chelated by adding, for example, ethylenedinitrotetraacetic acid (EDTA) to the dissolution medium, or to the sample. To illustrate the severity of relaxation during dissolution [1-^{13}C]pyruvic acid (pyruvic acid enriched with ^{13}C to 99% in the C-1, ie, carboxylic acid, position) is chosen as an example. This molecule has been well studied with DNP and has high biological relevance. In Fig. 2 the

Table 1
Dissolution-DNP Compounds (97–106)

Agent	Products	Ref.
[1-^{13}C]pyruvate	[1-^{13}C]lactate, [1-^{13}C]alanine, [^{13}C] bicarbonate, $^{13}CO_2$	41
[2-^{13}C]pyruvate	[2-^{13}C]lactate, [2-^{13}C]alanine, [1-^{13}C]acetyl-carnitine, [1-^{13}C]citrate, [5-^{13}C]glutamate	92,95
[1,2-$^{13}C_2$]pyruvate	[1,2-$^{13}C_2$]lactate, [1,2-$^{13}C_2$]alanine, [1-^{13}C]acetyl-carnitine, [1-^{13}C]citrate, [5-^{13}C]glutamate, [^{13}C]bicarbonate, $^{13}CO_2$	100
[1-^{13}C]lactate	[1-^{13}C]pyruvate, [1-^{13}C]alanine, [^{13}C] bicarbonate, $^{13}CO_2$	101
13C-bicarbonate	$^{13}CO_2$	13
[1,4-$^{13}C_2$]fumarate	[1,4-$^{13}C_2$]malate	85
[1-^{13}C]acetyl-methionine	[1-^{13}C]methionine	102
[2-^{13}C]fructose	[1-^{13}C]fructose-6-phosphate	103
[5-^{13}C]glutamine	[5-^{13}C]glutamate	107
[1-^{13}C]ethylpyruvate	[1-^{13}C]pyruvate, [1-^{13}C]lactate, [1-^{13}C]alanine, [^{13}C] bicarbonate, $^{13}CO_2$	93
[1,1'-$^{13}C_2$]acetic anhydride	Multiple depending on reactant	104
[1-^{13}C]acetate	[1-^{13}C]acetylcarnitine	109
13C Urea	None	105
bis-1,1-(hydroxymethyl)-[1-13C]cyclopropane-d8 HP001	None	108
α-keto-[1-^{13}C]isocaproate	[1-^{13}C]leucine	83
[1-^{13}C]dehydro ascorbic acid	[1-^{13}C]ascorbic acid	97,98
[1-^{13}C]alanine	[1-^{13}C]lactate, [1-^{13}C]pyruvate, [^{13}C]bicarbonate	106

T_1 of the C-1 of [1-^{13}C]pyruvic acid at 9.4 T is given as a function of temperature (unpubl. data). It can be seen that the shortest T_1 is ~1.6 seconds at 0°C. With the trityl radical present (20 mmol/L) there will be an additional (dipolar) relaxation contribution from the electron spin. It can be seen that the contribution from the trityl is marginal, but shifts the minimum to a different temperature (correlation time). According to relaxation theory the minimum T_1 scales with B_0, which means that a minimum T_1 of 0.7 seconds should be expected during the dissolution in the 3 T polarizer field. The data illustrate that the nuclear spin during the dissolution should pass through this T_1 minimum on a much faster time scale to avoid a loss of polarization. The example illustrates that it is not unreasonable to expect that the loss of polarization during dissolution can be overcome, but that a fast and efficient dissolution process is needed. The severity of the problem will depend on the target spin and sample properties, but several parameters can be controlled, eg, the distance to other spins (labeling position), the abundance of other spins (full or partial deuteration), and the concentration of the EPA.

In most cases the EPA or Gd chelate do not cause significant relaxation after dissolution, and may also be safe to inject into animals. For preclinical imaging it is not required to remove the EPA. The same applies to the Gd chelate in case it is used in the formulation. However, the solution may undergo a filtration or chromatography step to remove the EPA involved in the DNP process. In case a Gd chelate has been added, this agent may be removed as well. The filtration can either be in-line with the dissolution process or a subsequent step. In either case the filtration is completed in a matter of a few seconds with insignificant loss of polarization or target molecule (unpubl. work).

Clinical Polarizer Requirements

Recently a DNP polarizer designed with sterile use intent was published (31). The key design criteria of this concept are:

1. To provide a sterile barrier to the product through a single use fluid path.
2. To eliminate consumption of liquid cryogens.
3. To increase throughput by having four independent parallel samples.
4. To increase the size of the individual DNP samples up to 2.0 mL.
5. To automate the operation and remove operator variability and interventions.
6. To add noncontact quality control (QC).

The above criteria are required for successful clinical translation of hyperpolarization. The future will reveal if these are adequate and can fulfill regulatory requirements as well as gain user acceptance. Most important, it should be emphasized that a sealed sterile fluid path for all components in the polarization and dissolution process (compounding) provides a concept that allows filling and sealing at a manufacturing site without the need to break this barrier at any point in the process until the point of product release by the QC system. Second, it has been demonstrated that a closed-cycle, sorption pump based cryogenic system served by a cryo-cooler was able to achieve a base temperature of less than 0.8 K. The lower temperature translated directly into a higher solid state polarization. Thus, the authors reached a solid state polarization of 35%–40% at 0.8 K and 3.35 T.

Dissolution-DNP Agents

Of the growing list of agents investigated in vivo using this method (Table 1), the most studied is

[1-^{13}C]pyruvate. This agent has shown great utility in oncology, as exemplified by studies showing correlations with disease progression (34) and early response to therapy (35). Research in cardiology (36) and brain (37) have also shown promise. [1-^{13}]pyruvate was also the first agent to be used in a human study of hyperpolarized metabolic imaging (1). This molecule illustrates a number of important features of an ideal agent for hyperpolarized metabolic imaging. First, as pyruvic acid, it is a liquid at room temperature and can directly solubilize enough EPA (15 mM trityl) for relatively fast polarization build-up (time constant of ~15 min at 1.4 K and 3.35 T), and relatively high polarization (>20%). The high concentration inherent in the choice of a neat liquid (~14 M for pyruvic acid) also yields a relatively high concentration after dissolution. As a result, this agent can be injected safely at 250 mM, in doses up to 0.43 mL/kg.

MNS Hardware

Standard clinical MR systems and coils are designed to transmit and receive radiofrequency (RF) signals at ^{1}H resonance frequency only. However, multinuclear spectroscopy (MNS) packages are available from most manufacturers of whole-body MR scanners. This option allows the system to perform MR experiments on nonproton nuclei of interest such as ^{13}C and ^{15}N (for simplicity, the remainder of this section focuses on hardware required for ^{13}C studies). An MNS package typically includes a broadband RF power amplifier, in addition to the standard ^{1}H narrowband amplifier, that amplifies the RF pulse waveforms to give them enough power through a transmit RF coil to create the necessary B_1 field at the resonance frequency of the nucleus of interest. This transmit RF coil could be a dedicated coil tuned to the resonance frequency for ^{13}C. The ^{13}C coil can be designed to perform both RF transmission and reception for ^{13}C, or designed to perform RF transmission only with a separate coil(s) for RF reception, also tuned to the ^{13}C resonance frequency. Whether the reception of the MR signal is performed by a dedicated RF receive coil(s) or by a transmit/receive coil, the signal is amplified by a preamplifier prior to digitization, processing, and image reconstruction. The preamplifiers typically work at a narrow range of frequencies and can be built into the MR scanner or into the RF coil, with one preamplifier generally required for each receive channel. Thus, to perform ^{13}C experiments, dedicated preamplifiers that operate at the ^{13}C frequency need to be either added to the system or built into the ^{13}C coils.

Since it is desirable to perform both ^{1}H anatomical imaging and hyperpolarized ^{13}C metabolic imaging during the same exam without repositioning the subject, the ^{13}C RF coil design and setup need to preserve the ability to perform ^{1}H imaging with a minimal compromise of image quality. Volume coils that can operate at both ^{1}H and ^{13}C frequencies (dual-tuned) have been demonstrated for preclinical hyperpolarized ^{13}C imaging (34,38). The coil configuration and design can be further optimized for imaging a particular organ/anatomy. For example, in the first proof-of-concept clinical trial of hyperpolarized ^{13}C metabolic imaging in prostate cancer patients, a ^{13}C transmit-only volume coil built into a custom patient table was used in conjunction with a receive-only endorectal coil that contained both a ^{13}C and a ^{1}H element for signal reception and the system body coil was used for ^{1}H RF transmission during ^{1}H imaging (39). A multichannel ^{13}C receive-only array coil suited for other human applications has also been demonstrated recently (40). Regardless of the coil design and combination, the MR system needs to be configured so that the correct coils/channels are active or disabled during specific periods of the scans to avoid signal degradation due to coupling. The gradient coils existing on all MR scanners to provide spatially varying magnetic fields to allow localization of RF signals can be used for ^{13}C imaging without any hardware modification. However, it is important to note that for a given magnetic field gradient the spatial variation in resonance frequency experienced by the nucleus is proportional to its gyromagnetic ratio. Thus, the highest spatial resolution achievable for ^{13}C imaging is approximately one-fourth that of ^{1}H under the same imaging conditions; the designs and implementations of RF pulse sequences for ^{13}C imaging need to take this limitation into consideration. It is possible to circumvent the low gyromagnetic ratio limitation by transferring the ^{13}C or ^{15}N magnetization to neighboring ^{1}H nuclei for detection (41,42). But simultaneous RF transmission at both ^{1}H and the low γ nucleus frequencies is required for the polarization transfer pulse sequence, and this capability may not be available on some clinical MR systems even with MNS package installed.

Nonrecoverable Magnetization

The magnetization of hyperpolarized ^{13}C substrate is largely enhanced in the DNP polarizer. After dissolution, the liquid state polarization currently achievable is ~20% (or 200,000 ppm). Once dissolved, the hyperpolarized ^{13}C magnetization undergoes T_1 relaxation toward thermal equilibrium in a similar physical mechanism as water protons in the human body after an RF excitation or inversion in a typical MRI scan. But body protons *recover* to thermal equilibrium via T_1 relaxation, whereas the hyperpolarized ^{13}C substrate irreversibly *decays* into thermal equilibrium via T_1 relaxation. Once decayed, the 200,000 ppm hyperpolarized magnetization is not recoverable and the magnetization of the ^{13}C substrate remains at the thermal equilibrium level, about 2.6 ppm at 3 T. In addition to the loss of polarization due to T_1 relaxation, RF pulses deplete polarization in a nonrecoverable way. Hyperpolarized gas imaging using ^{3}He or ^{129}Xe also utilizes nonrecoverable magnetization, subject to T_1 relaxation and RF depletion. Thus, sample delivery and data acquisition in hyperpolarized imaging need to be sufficiently fast in order to utilize this decaying and nonrecoverable magnetization (for [1-^{13}C]pyruvate, most of the nonequilibrium polarization is lost within 2–3 minutes postdissolution). However, different from hyperpolarized gases, some

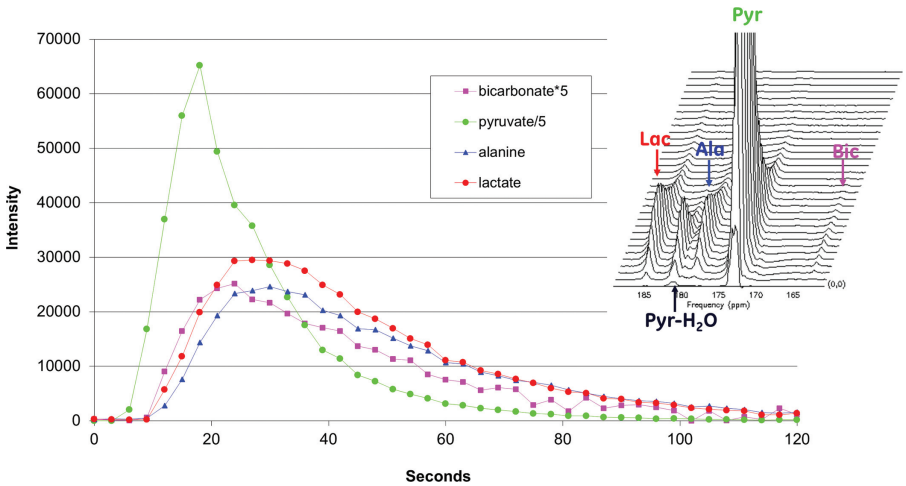

Figure 3. Dynamic curves of ^{13}C-pyruvate, and its metabolic products: ^{13}C-alanine, ^{13}C-lactate, and ^{13}C-bicarbonate (as labeled), following an injection of hyperpolarized [1-^{13}C]pyruvate into a rat. The dynamic signals were obtained from the individual peak height of a stack of spectra (right insert) acquired every 3 seconds from a 90-mm thick section of the rat torso.

hyperpolarized ^{13}C substrates such as [1-^{13}C]pyruvate also undergo metabolic conversions to downstream metabolites. Therefore, the signal-to-noise ratio (SNR) of hyperpolarized ^{13}C in vivo depends on the T_1 relaxation time, metabolic conversion rates, liquid state polarization, concentration, agent delivery time, acquisition timing, and pulse sequence strategies of utilizing the nonrecoverable magnetization. The following section describes the most popular data acquisition strategies for hyperpolarized ^{13}C imaging.

Pulse Sequences

Hyperpolarized ^{13}C MRI typically requires acquisition of ^{13}C signals from the injected metabolite and its metabolic products. These ^{13}C-labeled metabolites can be observed as a spectrum of peaks at different resonance frequencies. Both the spatial distribution and temporal evolution of the metabolite signals are of a strong interest for understanding the dynamic metabolic process in vivo. Pulse sequence design progressed rapidly from single-slice, single-timepoint acquisition to five-dimensional MRSI: temporal, spectral, and three spatial dimensions. Optimizing sampling efficiency of nonrecoverable magnetization has been the primary focus of pulse sequence development for hyperpolarized ^{13}C MRSI. Methods such as compressed sensing and iterative decomposition of water and fat with echo asymmetry and least square estimation (IDEAL) have been applied to accelerate acquisitions in this context, and various RF pulse designs have been used to optimize SNR and/or contrast-to-noise ratio (CNR). In addition, there are specialty sequences for quantitation of T_2 and metabolic kinetics.

Single Timepoint MRSI

Early work in hyperpolarized ^{13}C MRSI employed concentric phase encoding and variable flip angle (38,43–45) techniques to acquire chemical shift images (CSI) in two dimensions within a short time window that coincides with the maximum ^{13}C signals of metabolic products. For these single timepoint images, the optimum acquisition depends on the bolus injection, the organ of interest, and perfusion. Therefore, a nonspatially resolved dynamic scan of the same region (Fig. 3) was often performed (in a separate bolus injection) prior to the imaging study to gain timing information from the metabolic signal–time curves (38). For a typical protocol of a 16 × 16 matrix and 5 × 5 mm in-plane resolution, it requires 15–20 seconds to acquire CSI of a single slice because of the long readout duration (to obtain adequate spectral resolution) and one TR is needed for each spatial encoding point in X and Y. Higher spatial resolution is possible in the same scan time, but requires a smaller field of view (FOV), which may result in spatial aliasing in clinical settings unless the ^{13}C coil receptivity profile limits the FOV, such as is the case for surface coils or endorectal coils.

Rapid CSI techniques have been developed to improve sampling efficiency within the available time window. Echo-planar spectroscopic imaging (EPSI) with flyback (46) or symmetric gradient waveform (47) traverses time and one spatial frequency domain in a single readout period, shortening the acquisition and allowing either single-timepoint 3D MRSI or time-resolved multislice 2D MRSI (34,45) on a standard clinical 3 T system (with a maximum gradient strength of 4 G/cm and slew rate of 150 mT/m/ms). There is a trade-off between spectral bandwidth and spatial resolution in the design of these gradient trajectories. Typically, a 5-mm resolution is achievable with 500 Hz spectral bandwidth without spectral aliasing of [1-^{13}C]pyruvate and its metabolic products (except ^{13}C bicarbonate). A similar trade-off also exists for spiral CSI (48), which employs spiral readout gradients to sample X and Y simultaneously, and concatenates the spiral gradients multiple times for chemical shift encoding. However, even with multiple interleaves to minimize the impact of gradient slew-rate, the 2D spiral readout time can result in a spectral bandwidth that is insufficient to fully cover the metabolite chemical shift range. This causes spectral aliasing, which needs to be corrected in the image reconstruction (48,49) or otherwise, results in image blurring. On a clinical system, spiral CSI completes a 2D MRSI of a single slice in 375 msec, a 50-fold reduction in scan time (50) compared to the

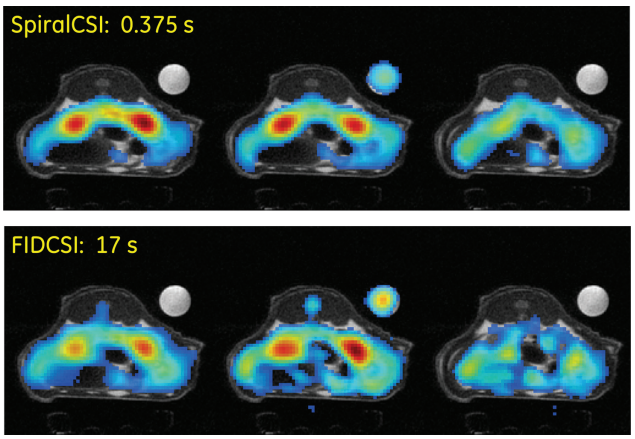

Figure 4. Comparison of spiral CSI and conventional FIDCSI. Images were obtained from a single slice rat kidney for [1-^{13}C]pyruvate (left), [1-^{13}C]lactate (middle), and [1-^{13}C]alanine (right). Spiral CSI (0.375 sec per slice) than FIDCSI (17 sec per slice) with similar image quality. Courtesy of Dr. Dirk Mayer of SRI, International and Stanford University.

conventional CSI method (Fig. 4). However, for clinical applications that require a large FOV, spiral CSI acquisition time may increase drastically due to the increase of interleaves required to maintain the same spatial resolution and spectral bandwidth. In addition, spiral CSI encodes a circular FOV and can become inefficient for a region of interest (ROI) with an asymmetric FOV. On the other hand, EPSI allows asymmetric FOV and the FOV in the one direction encoded by the EPSI readout is virtually unlimited due to the very high sampling rate available on all clinical systems.

Acceleration to 5D MRSI

When the information of temporal dynamics and spatial distribution are both needed, time-resolved MRSI with multislice 2D or 3D volumetric coverage is a good strategy. Time-resolved metabolic data can be used to determine rate constants (51), and signal averaging over the time course for each voxel can regain most of the SNR observed in optimized non-time-resolved methods. In preclinical studies, 5D MRSI has been demonstrated by using spiral CSI (51,52) and compressed sensing (53,54), both yielding high-quality images and dynamic curves. Taking advantage of the considerable sparsity in hyperpolarized ^{13}C spectra, compressed sensing pseudorandomly undersampled spectral and X-Y spatial domains during EPSI flyback readout, yields up to a factor of 7.53 in acceleration (55) relative to the conventional 3D EPSI sequence (46) (Fig. 5). The acceleration can be used to improve spatial resolution and decrease acquisition time, or to cover a larger FOV, which will be useful for clinical applications. The trade-off of this technique is the loss of metabolite peaks with low SNR (appears to break down for SNR less than ~7). This could potentially limit its applications depending on the achievable clinical SNR, which is yet to be determined by clinical trials.

Another approach under development is IDEAL spiral CSI (56), using the iterative least-squares chemical shift-based (LSCS) method. This technique has been used clinically for decompositions of water from fat (57), but is also capable of decomposing multiple ^{13}C-labeled chemical species (58). Spectral sampling is accomplished by shifting the echo time (TE) from excitation to excitation and 2D images at each TE are acquired by using spiral gradient trajectories. IDEAL requires a priori information of chemical shift frequencies of ^{13}C metabolite peaks and, with such, IDEAL allows minimum numbers of excitations for spectral decomposition, an efficient sampling strategy for a sparse spectrum over a wide bandwidth. There is no trade-off between spatial resolution and spectral bandwidth and, therefore, the spatial resolution can be as high as SNR permits. This technique has been demonstrated in time-resolved 2D imaging, with a potential of combining with a pulse-and-acquire FID acquisition to obtain a pseudo spectrum (59). The integrity of the pseudo spectrum obtained by using this technique for quantitation purposes is under investigation in preclinical studies.

RF Designs to Optimize SNR

The signal of the injected, relatively concentrated, hyperpolarized ^{13}C substrate is often 5 to 10 times larger than the signals of its metabolic products

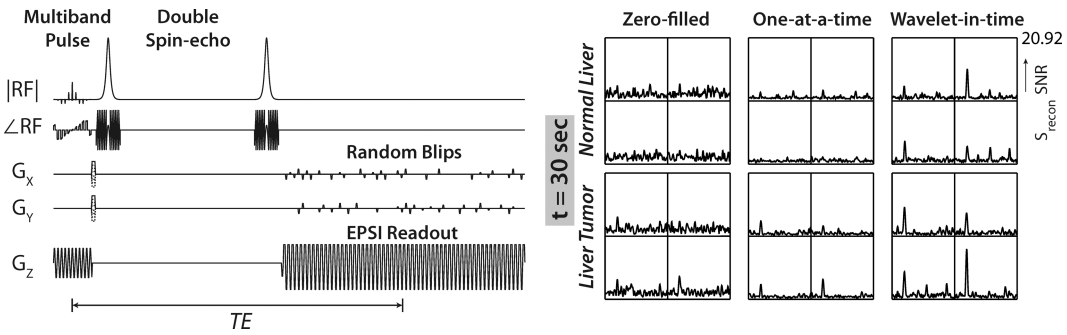

Figure 5. Pulse diagram of multiband and compressed sensing sequence (left), and reconstructed spectra (right) of time-resolved 3D MRSI data. Improved peak detection of the wavelet-in-time method is most evident at 30 seconds after hyperpolarized [1-^{13}C]pyruvate injection. Courtesy of Dr. Peder Larson, Dr. Simon Hu, and Dr. Dan Vigneron, University of California at San Francisco.

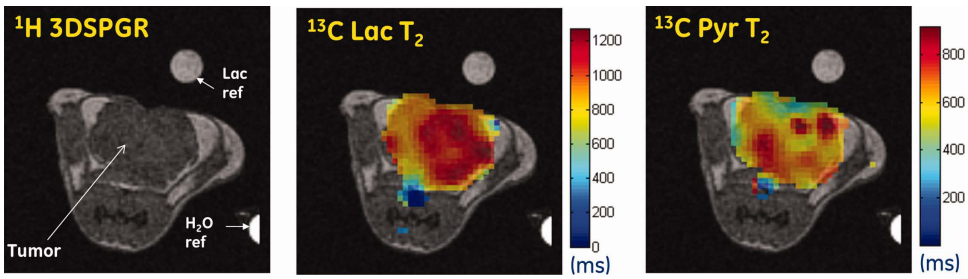

Figure 6. Quantitative ^{13}C-lactate (middle) and ^{13}C-pyruvate (right) T_2 maps of a single 2 mm slice on TRAMP tumor. Tumor appears homogeneous on proton 3D-SPGR image (left) but has heterogeneous T_2 values for [1-^{13}C]lactate and [1-^{13}C]pyruvate. The estimated T_2 errors range from 100 to 200 msec (not shown). [Color figure can be viewed in the online issue, which is available at wileyonlinelibrary.com.]

initially, whereas the product signals are replenished during the acquisition via recirculation of the surplus ^{13}C substrate. Multiband spectral-spatial RF excitation pulses (60) use spectral selectivity to minimally excite the injected hyperpolarized ^{13}C substrate while exciting the metabolic products with a larger flip angle to obtain higher SNR of the metabolites without saturating the substrate magnetization prematurely. The metabolic products are observable for a longer window and with better SNR than a uniformly constant flip angle (60) strategy. A recent development combining multiband RF pulse design and compressed sensing random sampling created a sequence for time-resolved 3D MRSI acquisition (55,61) with good SNR. The flip-angle of the injected ^{13}C substrate and that of the products can be optimized for optimal CNR ratio for a particular organ or for disease characterization (62).

An alternative to spectroscopically resolving multiple metabolites is direct imaging of each metabolite after selective excitation by a spectral-spatial pulse (63). Recently, a multislice cardiac-gated sequence consisting of a large flip-angle spectral-spatial excitation RF pulse with a single-shot spiral trajectory was developed for ^{13}C imaging of cardiac metabolism (64). The sequence alternates among the chemical shift frequencies corresponding to each metabolite and allows for rapid imaging of each individual metabolite.

T_2-Based Sequences

Long T_2 relaxation time of ^{13}C metabolites was first observed using a TRAMP (transgenic adenocarcinoma of the mouse prostate) tumor model (65). The T_2 difference between tumor and normal tissue was explored in a rat hepatocellular carcinoma (HCC) study (66) using a single-voxel preparation pulse followed by a train of spin-echoes to measure the T_2 decay of the signal within the voxel. T_2's of [1-^{13}C]alanine and [1-^{13}C]lactate were found to be longer in HCC tumors (1.2 sec and 0.9 sec, respectively) than in normal liver (0.4 sec and 0.5 sec, respectively). Recently, a T_2 mapping sequence was developed to measure T_2 of ^{13}C-labeled metabolites pixel-by-pixel with high resolution (67). T_2 values were extracted from regions of interest on the T_2 maps with better precision. Figure 6 shows the T_2 map of a single-slice acquired through a TRAMP tumor and the tumor has a T_2 of 1.4 seconds. The large T_2 difference between tumor and normal tissues presents an opportunity for greater imaging contrast when using a T_2-based sequence. A large SNR gain is also expected by using T_2-based sequences as compared to T_2^*-based sequences. For example, most of the sequences mentioned before are limited by signal loss caused by T_2^* decay. T_2^* can be as long as 100–200 msec for [1-^{13}C]pyruvate, but is reduced to about 25 msec for [1-^{13}C]lactate and [1-^{13}C]alanine due to stronger J_{CH} coupling (38), and all these T_2^* values are shorter than the T_2 values. T_2-based sequences, such as multiecho balanced-steady-state free precession (SSFP) (68,69) and stabilized fast spin echo (FSE)-EPSI (70), have significant signal gain and are excellent for single-timepoint MRSI. The challenge to utilize this strategy for time-resolved MRSI lies in the strong RF depletion during the echo train. Multiecho balanced-SSFP has been demonstrated in 3D acquisition for time-resolved hyperpolarized chemical shift imaging (71), but the temporal resolution of 16 seconds may not be sufficient for characterizing the metabolic dynamics.

Kinetic Modeling

Hyperpolarized pyruvate-to-lactate signal-time curves have been described by two-site exchange (35,72) models. Under saturating conditions, the apparent rate constant *Kpl* increases as the pyruvate dose decreases (72). The small tip-angle, pulse-and-acquire dynamic curves are biased by the substrate dose, bolus shape, and accumulated in flow of [1-^{13}C]lactate. These factors can be eliminated by using a saturation recovery method (67,68), resulting in dynamic curves that describe the instantaneous metabolic conversion at the local tissue level during the passage of hyperpolarized [1-^{13}C]pyruvate. This method typically consists of multiple 90°-excitations to acquire dynamic spectroscopic images and spectrally selective saturation pulses applied in between acquisition of time frames to spoil the inflow of [1-^{13}C]lactate while preserving inflow of fresh [1-^{13}C]pyruvate. The resulting kinetic data were fully sampled at each timepoint and were unbiased by the substrate dose, bolus shape, and product decay. Apparent maximal reaction velocity V_{max} and asymptotic conversion rate at saturated condition K_M can be derived by kinetic modeling of the saturation recovery dynamic curves (67).

Exchange vs. Flux

The conversion of [1-^{13}C]pyruvate to [1-^{13}C]lactate, as observed in hyperpolarized metabolic imaging, is a combination of flux (net creation of lactate) and exchange (^{13}C enrichment of the lactate pool with no net change in concentration). In whole blood, pyruvate-lactate exchange occurs at a rate 3–5 times the rate of flux (73). The impact of lactate pool size and exchange was demonstrated for hyperpolarized [1-^{13}C]pyruvate metabolic spectroscopy using cells preconditioned with unlabeled lactate (35). Under conditions of elevated steady-state lactate (unlabeled), a large increase in hyperpolarized [1-^{13}C]lactate was observed. Recently, the importance of exchange has been demonstrated in a lymphoma model, under the high bolus concentration hyperpolarized [1-^{13}C]pyruvate and magnetization transfer technique (74). The authors of this study further concluded that steady-state lactate pool size is the likely limit of detection for [1-^{13}C]lactate in regions-of-interest such as blood and muscle.

The availability of the reduced form of nicotinamide adenine dinucleotide NADH, from sources beyond lactate dehydrogenase (LDH) catalyzed exchange, also impacts the conversion of hyperpolarized [1-^{13}C]pyruvate to [1-^{13}C]lactate. For example, added NADH from aldolase processing of ethanol in liver (75), or from mitochondria via a reverse of the malate-aspartate shuttle (76), have been shown to increase the flux of hyperpolarized [1-^{13}C]pyruvate to [1-^{13}C]lactate. However, the balance of flux and exchange has not yet been quantitatively established, and remains to be determined, even for normal tissues and conditions.

APPLICATIONS

Oncology

Prostate Cancer

Initial experience in hyperpolarized ^{13}C metabolic imaging of prostate cancer was reported by Chen et al (45) by injecting hyperpolarized [1-^{13}C]pyruvate into transgenic adenocarcinoma of mouse prostate (TRAMP) model. The study showed highly elevated lactate signal in late-stage prostate tumors. Albers et al (34) compared hyperpolarized ^{13}C metabolic imaging of prostate cancer with histology. Normal mice and TRAMP of various histologic grades were studied. Images of ^{13}C-pyruvate, ^{13}C-lactate, and ^{13}C-alanine were obtained by using 3D EPSI sequence in 14 seconds. The lactate signal level increases with tumor progression and correlates strongly with histologic grade.

Clinical Trial

The first clinical trial of hyperpolarized ^{13}C-pyruvate metabolic imaging of prostate cancer patients was successfully conducted at the University of California in San Francisco (1). This study was a proof-of-concept trial entitled "A Phase 1/2a Ascending-Dose Study to Assess the Safety and Tolerability and Imaging Potential of Hyperpolarized Pyruvate (^{13}C) Injection in Subjects with Prostate Cancer." This 33-patient study was conducted with the primary objective to assess the safety of hyperpolarized pyruvate (^{13}C) injection in men with prostate cancer and intact prostates. The secondary objectives were to determine: 1) The kinetics of hyperpolarized pyruvate injection delivery and metabolism throughout the prostate, and 2) to determine the SNR for ^{13}C pyruvate metabolites and total hyperpolarized carbon (THC) in regions of cancer and in surrounding benign prostate as a function of the dose of the hyperpolarized pyruvate (^{13}C) injection. All doses were well tolerated without exception, and excellent CNR for [1-^{13}C]lactate was observed even at the lowest dose (private commun.).

Liver Metabolism and Hepatocellular Carcinoma

Using hyperpolarized [1-^{13}C]pyruvate, Hu et al (77) studied liver metabolism in fasted rats and found higher lactate-to-alanine signal ratios and lower alanine signal level in the fasted rats than in free-fed rats. The low alanine signal is most likely due to a reduction of alanine aminotransferase (ALT) activity in fasted rat liver during gluconeogenesis. Alanine is also a good biomarker for HCC detection. Using hyperpolarized [1-^{13}C]pyruvate, Darpolor et al (78) found elevated alanine and lactate levels, consistent with enzyme expression analysis on rat HCC tissue extract. Interestingly, ^{13}C MRSI showed high alanine signals specifically in HCC tumors, whereas it showed high lactate signals in the HCC tumors and in blood vessels. Low ^{13}C-alanine signals in vessels may be due to the much slower transport of alanine than lactate from cells to blood. Therefore, within the 1 minute of ^{13}C acquisition time window, not much ^{13}C-alanine signal was observed in vessels but only in HCC tumors. This is a promising technique for liver cancer diagnosis and treatment monitoring.

Glioma

Park et al (79) assessed the potential use of hyperpolarized ^{13}C-pyruvate for glioma prognosis in rat models. The signal levels of ^{13}C-pyruvate and its metabolic product, ^{13}C-lactate, as well as their relative signal ratios were significantly higher in tumors than in normal brain. The ^{13}C-lactate signal correlated with proliferation. The different ^{13}C metabolic profile between two different models in the study was consistent with their immunohistochemical data. Time-resolved 2D MRSI was reported recently in a rat glioma model, comparing metabolic conversion rates between glioma and normal brain (80). In both studies, large ^{13}C-pyruvate uptake was observed due to the disruption of the blood–brain barrier (BBB) in gliomas. For studies of ^{13}C-pyruvate metabolism in normal rat brain, where the BBB is intact, see the Neurology section below.

Lymphoma

Extracellular pH is known as a biomarker of interstitial lactic acid production (81). Although intracellular pH has been measured by ^{31}P MRS (82), the lower sensitivity of ^{31}P MRS limits its application for human studies with appropriate spatial resolution and

reasonable imaging time window. With the 5 orders of magnitude signal enhancement afforded by the DNP technique, Gallagher et al (13) mapped the pH of murine lymphoma tumor by applying ^{13}C MRSI following an injection of hyperpolarized ^{13}C-bicarbonate. The pH value in each voxel was calculated using the relative signal of ^{13}C-bicarbonate and its metabolic product $^{13}CO_2$ using the Henderson-Hasselbalch equation. The tumor showed lower pH than the surrounding healthy tissues.

Another hyperpolarized ^{13}C substrate that has been tested on lymphoma is 2-keto-[1-^{13}C]isocaproate (KIC). KIC is metabolized to leucine by branched chain amino acid transferase (BCAT), a biomarker for metastasis in some tumors and a target of proto-oncogene c-myc. Following injection of hyperpolarized KIC, Karlsson et al (83) found more than a 7-fold higher signal of ^{13}C-leucine in murine lymphoma than in healthy tissue. In the same study, no ^{13}C-leucine was observed in rat mammary adenocarcinoma. Ex vivo BCAT expression analysis yielded a high BCAT level in murine lymphoma and a very low BCAT level in rat mammary tumor, consistent with the hyperpolarized ^{13}C metabolic imaging findings.

Therapeutic Response

Day et al (35) reported decreased flux between pyruvate and lactate in lymphoma tumors when treated with etoposide and interrogated with hyperpolarized [1-^{13}C]pyruvate. The etoposide induces apoptosis and loss of NADH due to activation of poly (ADP-ribose) polymerase (PARP) leading to reduced LDH activity. This study is the benchmark to demonstrate the feasibility of using hyperpolarized ^{13}C metabolic MR to monitor early treatment effects.

A similar finding was also reported by Chen et al (84) in a study of treatment response on TRAMP tumors by using hyperpolarized [1-^{13}C]pyruvate. Reduced ^{13}C lactate to pyruvate ratio was found in the TRAMP mice that responded to androgen deprivation therapy and no change was found in the ratio in nonresponding mice.

In a study of treatment monitoring of lymphoma tumors using hyperpolarized [1,4-$^{13}C_2$]fumarate, Gallagher et al (85) found that production of [1,4-$^{13}C_2$]malate from the labeled fumarate is a sensitive marker of cellular necrosis. The conversion was 2.4-fold higher in etoposide-treated lymphoma tumors, where significant levels of tumor cell necrosis formed than in the untreated tumors. This technique has clinical potential for monitoring early therapeutic response.

Cardiology

Generation and utilization of adenosine triphosphate (ATP) in the heart are tightly controlled events regulated by physiological conditions and energetic needs. Normally, the heart uses fatty acids, carbohydrates, and ketones as the substrates for energy production. Altered myocardial substrate utilization is associated with diseases such as cardiomyopathy, hypertension, and diabetes; it also occurs during ischemia and reperfusion. Since all substrates are converted to acetyl-CoA prior to entering the Krebs cycle, measurement of the metabolic fluxes of acetyl-CoA production from various substrates can be used to monitor the changes in substrate selection and utilization. Pyruvate dehydrogenase (PDH) is the enzyme that decarboxylates the carbohydrate derived pyruvate to acetyl-CoA and CO_2, and the control of this enzyme's expression and activity is closely tied to myocardial substrate selection, thus the ability of using hyperpolarized ^{13}C pyruvate to noninvasively probe PDH flux is potentially a powerful diagnostic tool in cardiology.

Indeed, a number of recent reports in small and large animal models have demonstrated the ability of hyperpolarized ^{13}C MR imaging and spectroscopy to characterize the PDH flux noninvasively in normal hearts and hearts during ischemia-reperfusion and cardiac diseases (86–90). In normal hearts, the $^{13}CO_2$ derived from [1-^{13}C]pyruvate due to cardiac PDH flux is observed mostly as ^{13}C-bicarbonate (in equilibrium with $^{13}CO_2$) signal (Fig. 7) in MR spectroscopy data (64,87,88), and some [1-^{13}C]lactate and [1-^{13}C]alanine signals can also be observed. In spatially resolved ^{13}C MRI data obtained from large animal models, the substrate signal was found to be localized mostly in the cardiac chambers, while ^{13}C-bicarbonate was localized in the myocardium (Fig. 8); [1-^{13}C]lactate signal was more diffuse and observed in both the blood and cardiac muscle (64,86).

In models of ischemia and reperfusion, impaired PDH flux can be observed as decreased ^{13}C-bicarbonate signal shortly following reperfusion (86,89). Potentially, the viability of the affected tissue may be probed by following the recovery of the PDH flux (or the lack of it) post reperfusion and assessment of interventions targeting this metabolic pathway may also benefit from this technique. Changes in PDH flux due to diabetes have been investigated in a small animal model (88). Very recently it has also been reported that in a porcine pacing model of dilated cardiomyopathy (DCM) the disease progression can be followed noninvasively with ^{13}C metabolic imaging using hyperpolarized [1-^{13}C]pyruvate, and altered cardiac PDH flux was found to be strongly associated with onset of decompensated DCM (90). Monitoring cardiac substrate utilization in patients may provide valuable information regarding progression of these diseases and aid clinical management.

Although most of the efforts so far in utilizing hyperpolarized ^{13}C MR metabolic imaging in cardiology have been focused on probing substrate utilization using [1-^{13}C]pyruvate, the cardiac pH may also be assessed noninvasively by the $H^{13}CO_3^-/^{13}CO_2$ ratio and the Henderson-Hasselbalch equation (87,91), if sufficient SNR is obtained for the $^{13}CO_2$ signal. Monitoring of cardiac Krebs cycle flux in real time using hyperpolarized [2-^{13}C]pyruvate is also feasible since the C2 position on pyruvate is carried into the cycle through acetyl-CoA (instead of being released as $^{13}CO_2$), and changes of Krebs cycle flux can be assessed by measuring changes in the [5-^{13}C]glutamate signal (92). Along with PDH flux, these additional parameters obtainable by hyperpolarized ^{13}C

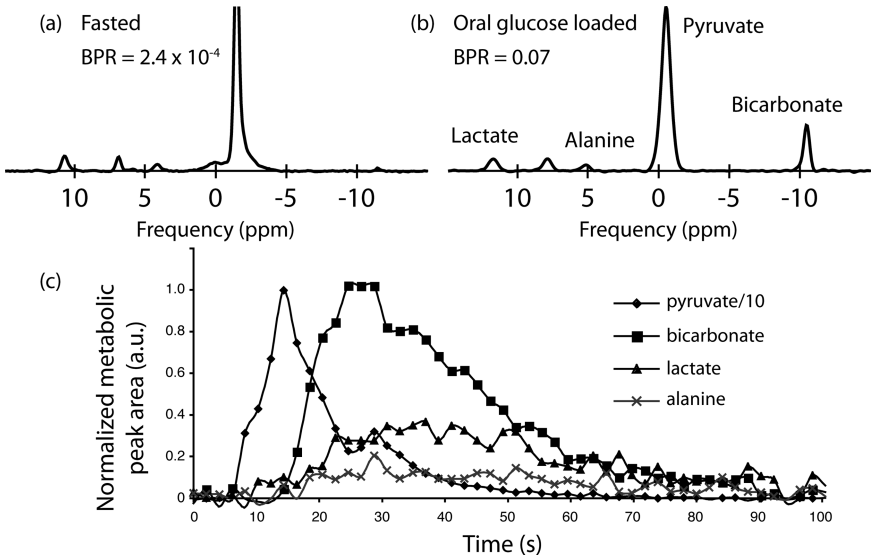

Figure 7. Cardiac-gated dynamic MRS data from pig hearts. **a**: Representative spectrum from the maximum bicarbonate frame in a fasted pig. **b**: Representative spectrum from the maximum bicarbonate frame in an oral glucose loaded pig. **c**: Time course of peak areas of pyruvate, bicarbonate, lactate, and alanine resonances acquired every 4 R-R intervals in the oral glucose loaded pig. The maximum bicarbonate to maximum pyruvate ratio (BPR) altered dramatically based on fed condition of the animal, due to changes in myocardial substrate utilization. Used with permission from Lau AZ, et al., Rapid multislice imaging of hyperpolarized (13)C pyruvate and bicarbonate in the heart. Magn Reson Med 2010;64:1323–1331, John Wiley & Sons.

MR provide insights into cardiac energetics and cellular environment that were not previously accessible noninvasively by other imaging modalities and may become valuable clinical tools in cardiology.

Neurology

The direct quantitative measures of BBB transport, inflammation, and oxidative load with hyperpolarized metabolic imaging has the potential to address unmet clinical needs in neurodegenerative disease, traumatic brain injury, and stroke. Unfortunately, this area of research trails the exciting progress that has been made in oncology and cardiology. Part of the lag in neurology may be due to the concern about the transport rate of T_1-limited hyperpolarized metabolic imaging agents through the BBB. One strategy to overcome the BBB transport limit explored the use of the

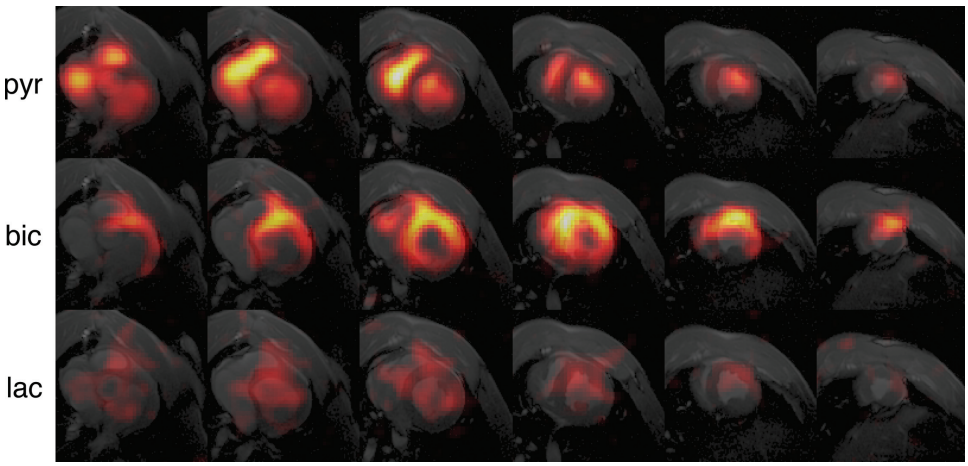

Figure 8. In vivo dynamic ^{13}C MRI data acquired using a multislice respiratory-gated spiral sequence showing spatial distribution of metabolites in a short-axis view of the heart. Pyruvate volume (six slices) were acquired starting from 10 seconds after the start of [1-^{13}C]pyruvate injection to capture the bolus through the heart (one volume of pyruvate images acquired during one respiratory cycle, 10 respiratory cycles of pyruvate data acquired, pyruvate images from peak of the bolus shown). Bicarbonate and lactate image volumes were acquired after the pyruvate bolus and were each repeated three times. The resolution of the overlaid reconstructed ^{13}C images is 10.7 mm in-plane for bicarbonate and pyruvate and 12 mm for lactate with a 1-cm slice thickness (pyruvate images are shown with a difference scale from bicarbonate and lactate images). The scan was completed in ~1 minute. Almost all the [1-^{13}C]pyruvate signal observed was localized in the blood while ^{13}C-bicarbonate was confined mostly in the heart muscle. Figure courtesy of Angus Z. Lau and Charles H. Cunningham of Sunnybrook Health Sciences Centre.

nonpolar precursor molecule, ethyl-pyruvate (93). This molecule is readily taken up by the brain and metabolized, but injection rate is limited, and interpretation is complicated by the rate of hydrolysis. However, as part of this study it was discovered that a substantial amount of [1-^{13}C]pyruvate does make it through normal BBB during the first passage of a bolus, and is converted to [1-^{13}C]lactate. Both ^{13}C-bicarbonate and [1-^{13}C]lactate appear to be formed in brain tissue (51,94,95). In a subsequent dynamic metabolic imaging study, the [1-^{13}C]lactate observed in a brain ROI was found to arise from brain metabolism, while the bulk of the [1-^{13}C]pyruvate observed in that same ROI appeared to arise from the cerebral blood volume (51). Since a substantial amount of [1-^{13}C]pyruvate makes it across the normal BBB and is converted to [1-^{13}C]lactate, it should be possible to quantitatively measure the full range of BBB transport abnormalities. The quantitative nature of the measure of total ^{13}C taken up, as well as the metabolic activity, could make [1-^{13}C]pyruvate metabolic imaging an ideal tool to study the full range of disease-induced disruptions in the BBB, even the subtle ones that have been reported for some nonenhancing MS lesions (96).

Beyond [1-^{13}C]pyruvate, one of the most interesting agents for the study of neurodegenerative disease may be [1-^{13}C]dehydroascorbic acid (DHA) (97,98). This molecule has been shown to rapidly cross the BBB (99), and the conversion rate of DHA to vitamin C is expected to be a direct marker for oxidative stress (97,98). A number of other dissolution DNP agents have also been studied in the brain including KIC and [1-^{13}C]acetate (see Table 1).

CONCLUSION

Dissolution-DNP-enabled metabolic imaging is still a relatively young field, with active preclinical research. This includes rapid discovery of new indications for the lead compound, hyperpolarized [1-^{13}C]pyruvate, as well as a robust exploration of new agents. The success of the first clinical proof-of-concept trial and the development of a clinical polarizer should enable the next steps toward clinical translation of this technology.

REFERENCES

1. Nelson SJ, Kurhanewicz J, Vigneron DB, et al. Proof of Concept Clinical Trial of Hyperpolarized C-13 in Patients with Prostate Cancer. In: Proc 20th Annual Meeting ISMRM, Melbourne; 2012 (abstract 274).
2. Ardenkjaer-Larsen JH, Fridlund B, Gram A, et al. Increase in signal-to-noise ratio of > 10,000 times in liquid-state NMR. Proc Natl Acad Sci U S A 2003;100:10158–10163.
3. Ardenkjaer-Larsen JH, Axelsson O, Golman K, Wistrand L-G, Leunbach I, Petersson S. PCT patent application number WO99/35508, priority date 5 January 1998.
4. Wolber J, Ellner F, Fridlund B, et al. Generating highly polarized nuclear spins in solution using dynamic nuclear polarization. Nucl Meth Phys Res 2004;526:173–181.
5. Overhauser AW. Polarization of nuclei in metals. Phys Rev 1953; 92:411–415.
6. Carver TR, Slichter CP. Polarization of nuclear spins in metals. Phys Rev 1953;92:212–213.
7. Abragam A. Overhauser effect in nonmetals. Phys Rev 1955;98: 1729–1735.
8. Jeffries CD. Polarization of nuclei by resonance saturation in paramagnetic crystals. Phys Rev 1957;108:164–165.
9. Abragam A, Goldman M. Order and disorder. Oxford, UK: Clarendon Press; 1982.
10. de Boer W, Borghini M, Morimoto K, Niinikoski TO, Udo F. Dynamic polarization of protons, deuterons, and carbon-13 nuclei: thermal contact between nuclear spins and an electron spin-spin interaction reservoir. J Low Temp Phys 1974;15:249–266.
11. de Boer WD, Niinikoski TO. Dynamic proton polarization in propanediol below 0.5K. Nucl Instr Meth 1974;114:495–498.
12. Lewis RJ S. Sax's dangerous properties of industrial materials. New York: John Wiley & Sons; 2000.
13. Gallagher FA, Kettunen MI, Day SE, et al. Magnetic resonance imaging of pH in vivo using hyperpolarized 13C-labelled bicarbonate. Nature 2008;453:940–943.
14. Jensen PR, in't Zandt R, Karlsson M, et al. In: Proc 16th Annual Meeting ISMRM, Toronto; 2008 (abstract 892).
15. Jensen PR, Karlsson M, Meier S, Duus JØ, Lerche MH. Hyperpolarized amino acids for in vivo assays of transaminase activity. Chem Eur J 2009;15:10010–10012.
16. Heckmann J, Meyer W, Radtke E, Reicherz G. Electron spin resonance and its implication of the maximum nuclear polarization of deuterated solid target materials. Phys Rev 2006;74:Art. No. 134418.
17. Benjamin PS, Fuminori H, Matsumoto K-I, et al. The chemistry and biology of nitroxide compounds. Free Radic Biol Med 2007; 42:1632–1650.
18. Eaton SS, Eaton GR, Berliner L. Part A: free radicals, metals, medicine, and physiology. Part B: methodology, instrumentation, and dynamics. Series: Biological Magnetic Resonance. J Biomed EPR 2005;23/24.
19. Thaning M. PCT patent application number WO 2006/011811 A2, priority date 30 July 2004.
20. Andersson S, Radner F, Rydbeck A, Servin R, Wisrand L-G. United States patent number US5728370, priority date 5 January 1998.
21. Reddy T, Iwama T, Halpern HJ, Rawal VH. General synthesis of persistent trityl radicals for EPR imaging of biological systems. J Org Chem 1998;67:4635–4639.
22. Bowman MK, Mailer C, Halpern HJ. The solution conformation of triarylmethyl radicals. J Magn Reson 2005;172:254–267.
23. Hu K-N, Bajaj VS, Rosay M, Griffin RG. High-frequency dynamic nuclear polarization using mixtures of TEMPO and trityl radicals. J Chem Phys 2007;126:044512.
24. Ardenkjaer-Larsen JH, Macholl S, Johannesson H. Dynamic Nuclear polarization with trityls at 1.2K. Appl Magn Reson 2008;34:509–522.
25. Duijvestijn MJ, Wind RA, Smidt J. Quantitative investigation of the dynamic nuclear polarization effect by fixed paramagnetic centra of abundant and rare spins in solids at room temperature. Physica B, C 1986;138:147–170.
26. Bajaj VS, Hornstein MK, Kreischer KE, et al. 250 GHz CW gyrotron oscillator for dynamic nuclear polarization in biological solid state NMR. J Magn Reson 2007;189:251–279.
27. Hornstein MK, Bajaj VS, Kreischer KE, Griffin RG, Temkin RJ. CW second harmonic results at 460 GHz of a gyrotron oscillator — for sensitivity enhanced NMR. The Joint 30th International Conference of Infrared and Millimeter Waves and 13th International Conference on Terahertz Electronics 2005;2:437–438.
28. Comment A, van der Brandt B, Uffmann K, et al. Design and performance of a DNP prepolarizer coupled to a rodent MRI scanner. Conc Magn Reson 2007;31:255–269.
29. Jannin S, Comment A, Kurdzesau F, et al. A 140 Ghz prepolarizer for dissolution dynamic nuclear polarization. J Chem Phys 2008;128:241102.
30. Johannesson H, Macholl S, Ardenkjaer-Larsen JH. Dynamic Nuclear Polarization of [1–13C]pyruvic acid at 4.6 Tesla. J Magn Reson 2008;197:167–175.
31. Ardenkjaer-Larsen JH, Leach AM, Clarke N, Urbahn J, Anderson D Skloss TW. Dynamic nuclear polarization polarizer for sterile use intent. NMR Biomed 2011;24:927–932.
32. Goertz, S. Spintemperatur und magnetische Resonanz verdünnter elektronischer Systeme — ein Weg zur Optimierung

polarisierter Festkörper-Targetmaterialien, Ruhr-Universität Bochum, Habilitationsschrift, April 15, 2002.
33. Jain J, Dey S, Muralidharan L, Leach AM, Ardenkjaer-Larsen JH. Jet impingment melting with vaporization: A numerical study. Proceedings of the ASME Summer Heat Transfer Conference, HT 2008, 559–567.
34. Albers MJ, Bok R, Chen AP, et al. Hyperpolarized 13C lactate, pyruvate, and alanine: noninvasive biomarkers for prostate cancer detection and grading. Cancer Res 2008;68:8607–8615.
35. Day SE, Kettunen MI, Gallagher FA, et al. Detecting tumor response to treatment using hyperpolarized 13C magnetic resonance imaging and spectroscopy. Nat Med 2007;13:1382–1387.
36. Schroeder MA, Clarke K, Neubauer S, Tyler DJ. Hyperpolarized magnetic resonance: a novel technique for the in vivo assessment of cardiovascular disease. Circulation 2011;124:1580–1594.
37. Hurd RE, Yen YF, Mayer D, et al. Metabolic imaging in the anesthetized rat brain using hyperpolarized [1–13C] pyruvate and [1–13C] ethyl pyruvate. Magn Reson Med 2010;63:1137–1143.
38. Kohler SJ, Yen Y, Wolber J, et al. In vivo 13 carbon metabolic imaging at 3T with hyperpolarized 13C-1-pyruvate. Magn Reson Med 2007;58:65–69.
39. Tropp J, Calderon P, Carvajal L, et al. An endorectal dual frequency 13C-1H receive only probe for operation at 3.0 Tesla. In: Proc 14th Annual Meeting ISMRM, Seattle; 2006 (abstract 2594).
40. Tropp J, Lupo JM, Chen A, et al. Multi-channel metabolic imaging, with SENSE reconstruction, of hyperpolarized [1-(13)C] pyruvate in a live rat at 3.0 Tesla on a clinical MR scanner. J Magn Reson 2011;208:171–177.
41. Barb AW, Hekmatyar SK, Glushka JN, Prestegard JH. Exchange facilitated indirect detection of hyperpolarized 15ND2-amido-glutamine. J Magn Reson 2011;212:304–310.
42. Harris T, Giraudeau P, Frydman L. Kinetics from indirectly detected hyperpolarized NMR spectroscopy by using spatially selective coherence transfers. Chemistry 2010;17:697–703.
43. Golman K, in't Zandt R, Thaning M. Real-time metabolic imaging. Proc Natl Acad Sci U S A 2006;103:11270–11275.
44. Golman K, in't Zandt R, Lerche M, Pehrson R, Ardenkjaer-Larsen JH. Metabolic imaging by hyperpolarized 13C magnetic resonance imaging for in vivo tumor diagnosis. Cancer Res 2006;66:10855–10860.
45. Chen AP, Albers MJ, Cunningham CH, et al. Hyperpolarized C-13 spectroscopic imaging of the TRAMP mouse at 3T-initial experience. Magn Reson Med 2007;58:1099–1106.
46. Cunningham CH, Chen AP, Albers MJ, et al. Double spin-echo sequence for rapid spectroscopic imaging of hyperpolarized 13C. J Magn Reson 2007;187:357–362.
47. Yen YF, Kohler SJ, Chen AP, et al. Imaging considerations for in vivo 13C metabolic mapping using hyperpolarized 13C-pyruvate. Magn Reson Med 2009;62:1–10.
48. Mayer D, Levin YS, Hurd RE, Glover GH, Spielman DM. Fast metabolic imaging of systems with sparse spectra: application for hyperpolarized 13C imaging. Magn Reson Med 2006;56: 932–937.
49. Levin YS, Mayer D, Yen YF, Hurd RE, Spielman DM. Optimization of fast spiral chemical shift imaging using least squares reconstruction: application for hyperpolarized (13)C metabolic imaging. Magn Reson Med 2007;58:245–252.
50. Mayer D, Yen YF, Levin YS, et al. In vivo application of sub-second spiral chemical shift imaging (CSI) to hyperpolarized 13C metabolic imaging: comparison with phase-encoded CSI. J Magn Reson 2010;204:340–345.
51. Hurd RE, Yen YF, Tropp J, Pfefferbaum A, Spielman DM, Mayer D. Cerebral dynamics and metabolism of hyperpolarized [1-(13)C]pyruvate using time-resolved MR spectroscopic imaging. J Cereb Blood Flow Metab 2010;30:1734–1741.
52. Mayer D, Yen YF, Tropp J, Pfefferbaum A, Hurd RE, Spielman DM. Application of subsecond spiral chemical shift imaging to real-time multislice metabolic imaging of the rat in vivo after injection of hyperpolarized 13C1-pyruvate. Magn Reson Med 2009;62:557–564.
53. Lustig M, Donoho D, Pauly JM. Sparse MRI: the application of compressed sensing for rapid MR imaging. Magn Reson Med 2007;58:1182–1195.
54. Hu S, Lustig M, Chen AP, et al. Compressed sensing for resolution enhancement of hyperpolarized 13C flyback 3D-MRSI. J Magn Reson 2008;192:258–264.
55. Larson PE, Hu S, Lustig M, et al. Fast dynamic 3D MR spectroscopic imaging with compressed sensing and multiband excitation pulses for hyperpolarized (13)C studies. Magn Reson Med 2010;65:610–619.
56. Wiesinger F, Menzel MI, Weidl E, Janich M, Schwaiger M, Schulte RF. Minimum-norm IDEAL spiral CSI for efficient hyperpolarized 13C metabolic imaging. In: Proc 18th Annual Meeting ISMRM, Stockholm; 2010 (abstract 3290).
57. Reeder SB, Pineda AR, Wen Z, et al. Iterative decomposition of water and fat with echo asymmetry and least-squares estimation (IDEAL): application with fast spin-echo imaging. Magn Reson Med 2005;54:636–644.
58. Reeder SB, Brittain JH, Grist TM, Yen YF. Least-squares chemical shift separation for (13)C metabolic imaging. J Magn Reson Imaging 2007;26:1145–1152.
59. Wiesinger F, Weidl E, Menzel MI, et al. IDEAL spiral CSI for dynamic metabolic MR imaging of hyperpolarized [1–13C]pyruvate. Magn Reson Med 2011;25:142–151.
60. Larson PE, Kerr AB, Chen AP, et al. Multiband excitation pulses for hyperpolarized 13C dynamic chemical-shift imaging. J Magn Reson 2008;194:121–127.
61. Larson PE, Bok R, Kerr AB, et al. Investigation of tumor hyperpolarized [1–13C]-pyruvate dynamics using time-resolved multiband RF excitation echo-planar MRSI. Magn Reson Med 2010; 63:582–591.
62. Josan S, Hurd RE, Kerr AB, et al. Effects of RF excitation scheme on signal-to-noise-ratio and apparent rate constant estimation in dynamic volumetric imaging of hyperpolarized [1–13C]-pyruvate. In: Proc 19th Annual Meeting ISMRM, Montreal; 2011 (abstract 3528).
63. Cunningham CH, Chen AP, Lustig M, et al. Pulse sequence for dynamic volumetric imaging of hyperpolarized metabolic products. J Magn Reson 2008;193:139–146.
64. Lau AZ, Chen AP, Ghugre NR, et al. Rapid multislice imaging of hyperpolarized 13C pyruvate and bicarbonate in the heart. Magn Reson Med 2010;64:1323–1331.
65. Yen YF, Le Roux P, Bok R, et al. Apparent T2 of 13C-labeled metabolites in vivo. In: Proc 16th Annual Meeting ISMRM, Toronto; 2008 (abstract 1747).
66. Yen YF, Le Roux P, Mayer D, et al. T(2) relaxation times of (13)C metabolites in a rat hepatocellular carcinoma model measured in vivo using (13)C-MRS of hyperpolarized [1-(13)C]pyruvate. NMR Biomed 2010;23:414–423.
67. Yen YF, Josan S, Senadheera L, et al. Hyperpolarized 13C T2 Mapping. Experimental NMR Conference. Pacific Grove, CA; 2011 (abstract 138).
68. Leupold J, Mansson S, Petersson JS, Hennig J, Wieben O. Fast multiecho balanced SSFP metabolite mapping of (1)H and hyperpolarized (13)C compounds. MAGMA 2009;22:251–256.
69. Leupold J, Wieben O, Mansson S, et al. Fast chemical shift mapping with multiecho balanced SSFP. MAGMA 2006;19:267–273.
70. Yen Y-F, Le Roux P, Bok R, et al. Signal enhancement in low-dose hyperpolarized 13C imaging using multi-slice FSEPSI sequence. In: Proc 16th Annual Meeting ISMRM, Toronto; 2008 (abstract 890).
71. Perman WH, Bhattacharya P, Leupold J, et al. Fast volumetric spatial-spectral MR imaging of hyperpolarized ^{13}C-labeled compounds using multiple echo 3D bSSFP. Magn Reson Imaging 2010;28:459–465.
72. Zierhut ML, Yen YF, Chen AP, et al. Kinetic modeling of hyperpolarized 13C1-pyruvate metabolism in normal rats and TRAMP mice. J Magn Reson 2010;202:85–92.
73. Romijn JA, Chinkes DL, Schwarz JM, Wolfe RR. Lactate-pyruvate interconversion in blood: implications for in vivo tracer studies. Am J Physiol 1994;266(3 Pt 1):E334–340.
74. Kettunen MI, Hu DE, Witney TH, et al. Magnetization transfer measurements of exchange between hyperpolarized [1–13C]pyruvate and [1–13C]lactate in a murine lymphoma. Magn Reson Med 2010;63:872–880.
75. Spielman DM, Mayer D, Yen YF, Tropp J, Hurd RE, Pfefferbaum A. In vivo measurement of ethanol metabolism in the rat liver using magnetic resonance spectroscopy of hyperpolarized [1–13C]pyruvate. Magn Reson Med 2009;62:307–313.
76. Moreno KX, Sabelhaus S, Merritt ME, Sherry D, Malloy CR. Malate-aspartate shuttle reversal allows for lactate concentration increases upon rapid changes in 13C pyruvate

concentration. In: Proc 18th Annual Meeting ISMRM, Stockholm; 2010 (abstract 1329).
77. Hu S, Chen AP, Zierhut ML, et al. In vivo carbon-13 dynamic MRS and MRSI of normal and fasted rat liver with hyperpolarized 13C-pyruvate. Mol Imaging Biol 2009;11:399–407.
78. Darpolor MM, Yen YF, Chua MS, et al. In vivo MRSI of hyperpolarized [1-(13) C]pyruvate metabolism in rat hepatocellular carcinoma. NMR Biomed 2011;24:506–513.
79. Park I, Larson PE, Zierhut ML, et al. Hyperpolarized 13C magnetic resonance metabolic imaging: application to brain tumors. Neuro Oncol 2010;12:133–144.
80. Park J, Josan S, Jang D, et al. Metabolic kinetics of a glioma model using hyperpolarized 13C magnetic resonance spectroscopic imaging. In: Proc 19th Annual Meeting ISMRM, Montreal; 2011 (abstract 3517).
81. Gillies RJ, Barry JA, Ross BD. In vitro and in vivo 13C and 31P NMR analyses of phosphocholine metabolism in rat glioma cells. Magn Reson Med 1994;32:310–318.
82. Stubbs M, Bhujwalla Z, Tozer G, et al. An assessment of 31P MRS as a method of measuring pH in rat tumours. NMR Biomed 1992;5:351–359.
83. Karlsson M, Jensen PR, in 't Zandt R, et al. Imaging of branched chain amino acid metabolism in tumors with hyperpolarized 13C ketoisocaproate. Int J Cancer 2010;127:729–736.
84. Chen AP, Bok R, Zhang V, et al. Serial hyperpolarized 13C 3D-MRSI following therapy in a mouse model of prostate cancer. In: Proc 16th Annual Meeting ISMRM, Toronto; 2008 (abstract 888).
85. Gallagher FA, Kettunen MI, Hu DE, et al. Production of hyperpolarized [1,4–13C2]malate from [1,4–13C2]fumarate is a marker of cell necrosis and treatment response in tumors. Proc Natl Acad Sci U S A 2009;106:19801–19806.
86. Golman K, Petersson JS, Magnusson P, et al. Cardiac metabolism measured noninvasively by hyperpolarized 13C MRI. Magn Reson Med 2008;59:1005–1013.
87. Merritt ME, Harrison C, Storey C, Jeffrey FM, Sherry AD, Malloy CR. Hyperpolarized 13C allows a direct measure of flux through a single enzyme-catalyzed step by NMR. Proc Natl Acad Sci U S A 2007;104:19773–19777.
88. Schroeder MA, Cochlin LE, Heather LC, Clark K, Radda GK, Tyler DJ. In vivo assessment of pyruvate dehydrogenase flux in the heart using hyperpolarized carbon-13 magnetic resonance. Proc Natl Acad Sci U S A 2008;105:12051–12056.
89. Merritt ME, Harrison C, Storey C, Sherry AD, Malloy CR. Inhibition of carbohydrate oxidation during the first minute of reperfusion after brief ischemia: NMR detection of hyperpolarized 13CO2 and H13CO3. Magn Reson Med 2008;60: 1029–1036.
90. Schroeder MA, Lau AZ, Chen AP, et al. Hyperpolarized 13C magnetic resonance imaging and spectroscopy uniquely reveal early and late onset metabolic changes in the failing heart. In: Proc 19th Annual Meeting ISMRM, Montreal; 2011 (abstract 21).
91. Schroeder MA, Swietach P, Atherton HJ, et al. Measuring intracellular pH in the heart using hyperpolarized carbon dioxide and bicarbonate: a 13C and 31P magnetic resonance spectroscopy study. Cardiovasc Res 2010;86:82–91.
92. Schroeder MA, Atherton HJ, Ball DR, et al. Real-time assessment of Krebs cycle metabolism using hyperpolarized 13C magnetic resonance spectroscopy. FASEB J 2009;23: 2529–2538.
93. Hurd RE, Yen YF, Mayer D, et al. Metabolic imaging in the anesthetized rat brain using hyperpolarized [1–13C] pyruvate and [1–13C] ethyl pyruvate. Magn Reson Med 2010;63:1137–1143.
94. Mayer D, Yen YF, Takahashi A, et al. Dynamic and high-resolution metabolic imaging of hyperpolarized [1-(13) C]-pyruvate in the rat brain using a high-performance gradient insert. Magn Reson Med 2011;65:1228–1233.
95. Marjanska M, Iltis I, Shestov AA, et al. In vivo 13C spectroscopy in the rat brain using hyperpolarized [1-(13)C]pyruvate and [2-(13)C]pyruvate. J Magn Reson 2010;206:210–218.
96. Soon D, Tozer D, Altmann D, Tofts P. Quantification of subtle blood-brain barrier disruption in non-enhancing lesions in multiple sclerosis: a study of disease and lesion subtypes. Multiple Sclerosis 2007;13:884–894.
97. Bohndiek SE, Kettunen MI, Hu DE, et al. Hyperpolarized [1-(13)c]-ascorbic and dehydroascorbic Acid: vitamin C as a probe for imaging redox status in vivo. J Am Chem Soc 2011;133: 11795–11801.
98. Keshari KR, Kurhanewicz J, Bok R, Larson PEZ, Vigneron DB, Wilson DM. Hyperpolarized 13C dehydroascorbate as an endogenous redox sensor for in vivo metabolic imaging. Proc Natl Acad Sci U S A 2011;29:1035–1040.
99. Huang J, Agus DB, Winfree CJ, et al. Dehydroascorbic acid, a blood-brain barrier transportable form of vitamin C, mediates potent cerebroprotection in experimental stroke. Proc Natl Acad Sci U S A 2001;98:11720–11724.
100. Chen A, Hurd R, Schroeder MA, et al. Simultaneous investigation of cardiac pyruvate dehydrogenase flux, Krebs cycle metabolism and intracellular pH using hyperpolarized [1,2–13C2] pyruvate. NMR Biomed 2012;25:305–311.
101. Chen AP, Kurhanewicz J, Bok R, et al. Feasibility of using hyperpolarized [1–13C]lactate as a substrate for in vivo metabolic 13C MRSI studies. Magn Reson Imaging 2008;26:721–726.
102. Chen AP, Hurd RE, Gu YP, Wilson DM, Cunningham CH. (13)C MR reporter probe system using dynamic nuclear polarization. NMR Biomed 2011;24:514–520.
103. Keshari KR, Wilson DM, Chen AP, et al. Hyperpolarized [2–13C]-fructose: a hemiketal DNP substrate for in vivo metabolic imaging. J Am Chem Soc 2009;131:17591–17596.
104. Wilson DM, Hurd RE, Keshari K, et al. Generation of hyperpolarized substrates by secondary labeling with [1,1–13C] acetic anhydride. Proc Natl Acad Sci USA 2009;106: 5503–5507.
105. Golman K, Ardenkjaer-Larsen JH, Petersson JS, Mansson S, Leunbach I. Molecular imaging with endogenous substances. Proc Natl Acad Sci U S A 2003;100:10435–10439.
106. Jensen PR, Karlsson M, Meier S, Duus JO, Lerche MH. Hyperpolarized amino acids for in vivo assays of transaminase activity. Chemistry 2009;15:10010–10012.
107. Gallagher FA, Kettunen MI, Day SE, et al. Detection of tumor glutamate metabolism in vivo using (13)C magnetic resonance spectroscopy and hyperpolarized [1-(13)C]glutamate. Magn Reson Med 2011;66:18–23.
108. Johansson E, Mansson S, Wirestam R, et al. Cerebral perfusion assessment by bolus tracking using hyperpolarized 13C. Magn Reson Med 2004;51:464–472.
109. Comment A, Uffmann K, Jannin A, et al. In vivo DNP-enhanced 13C labeled acetate brain studies in a 9.4T animal scanner. In: Proc 15th Annual Meeting ISMRM, Berlin; 2007 (abstract 369).